

HEATING THE INTRA-CLUSTER MEDIUM BY JET-INFLATED BUBBLES

Shlomi Hillel¹ and Noam Soker¹

ABSTRACT

We examine the heating of the intra-cluster medium (ICM) of cooling flow clusters of galaxies by jet-inflated bubbles and conclude that mixing of hot bubble gas with the ICM is more important than turbulent heating and shock heating. We use the `PLUTO` hydrodynamical code in full 3D to properly account for the inflation of the bubbles and to the multiple vortices induced by the jets and bubbles. The vortices mix some hot shocked jet gas with the ICM. For the parameters used by us the mixing process accounts for about four times as much heating as that by the kinetic energy in the ICM, namely, turbulence and sound waves. We conclude that turbulent heating plays a smaller role than mixing. Heating by shocks is even less efficient.

1. INTRODUCTION

A negative feedback mechanism determines the thermal evolution of the intra-cluster medium (ICM) in the inner regions of cooling flow (CF) clusters and groups of galaxies (McNamara & Nulsen 2007, 2012; some examples include Farage et al. 2012; Pfrommer 2013). This feedback mechanism is driven by active galactic nucleus (AGN) jets that inflate X-ray deficient cavities (bubbles; e.g., Dong et al. 2010; O’Sullivan et al. 2011; Gaspari et al. 2012a,b; Gilkis & Soker 2012). Examples of bubbles in cooling flows include Abell 2052 (Blanton et al. 2011), NGC 6338 (Pandge et al. 2012), NGC 5044 (David et al. 2009), and HCG 62 (Gitti et al. 2010), among many others.

Vortices inside the bubbles and in their surroundings play major roles in the formation of bubbles, their evolution, their interaction with the ICM, and the dynamics and formation of cold regions (e.g. Omma et al. 2004; Heinz & Churazov 2005; Roediger et al. 2007; Sternberg & Soker 2008b; Gilkis & Soker 2012). Some cool regions further cool and flow inward to feed the AGN. The process of feeding the AGN with cold clumps in the feedback mechanism cycle is termed the *cold feedback mechanism*, and was suggested by Pizzolato & Soker (2005). The cold feedback mechanism has been later strengthened by observations of cold gas and by more detailed studies (e.g., Revaz et al. 2008; Pope 2009; Pizzolato & Soker 2010; Edge et al. 2010; Wilman et al. 2011; Nesvadba et al. 2011; Cavagnolo et al. 2011; Gaspari et al. 2012a,b; McCourt et al. 2012; Sharma et al. 2012; Farage et al. 2012; Wagh et al. 2014; Banerjee & Sharma 2014; McNamara et al. 2014; Voit & Donahue 2015; Voit et al. 2015; Li et al. 2015; Prasad et al. 2015; Russell et al. 2015; Tremblay et al. 2015; Fogarty et al. 2015).

Gilkis & Soker (2012) and Hillel & Soker (2014) have shown that the mixing of the hot bubble gas with the ICM is a much more efficient heating process than heating by repeated shocks; hereafter termed shocks-heating. As the axis of the bubbles changes with time and/or the central jets’ source and the ICM move relative to each other, e.g., the galaxy group NGC 5813 (Randall et al. 2015), over time the mixing-heating

¹Department of Physics, Technion – Israel Institute of Technology, Haifa 32000, Israel; shlomihi@tx.technion.ac.il, soker@physics.technion.ac.il

operates in all directions. Shocks-heating is extremely inefficient, and is unlikely to explain the feedback mechanism (Soker et al. 2013). Randall et al. (2015) argue for shocks-heating in NGC 5813, ignoring the counter arguments for shocks-heating in NGC 5813 (Soker et al. 2013). We hold that even in NGC 5813 mixing is more important than shocks in heating the ICM (Soker et al. 2015). This heating by mixing closes the cycle in the cold feedback mechanism.

A key to the study of the mixing heating is to inflate bubbles self-consistently. This requires either slow (sub-relativistic) massive wide (SMW) jets (Sternberg et al. 2007), precessing jets (Sternberg & Soker 2008a; Falceta-Goncalves et al. 2010), or a relative motion of the jets to the medium (Brüggen et al. 2007; Soker 2009; Morsony et al. 2010; Mendenygral et al. 2012). In the present study we inflate bubbles by SMW jets, also supported by observations (e.g., Moe et al. 2009; Dunn et al. 2010; Arav et al. 2013), but our results hold for bubbles inflated by precessing jets or a relative motion of the ICM as well.

In a recent paper Zhuravleva et al. (2014) claim that heating by turbulence dominates in the Perseus cooling flow cluster. We here compare the energy that jet-inflated bubbles channel to turbulence and to the direct thermal energy of the ICM. The axi-symmetric 2D simulations of Gilkis & Soker (2012) and Hillel & Soker (2014) are insufficient to account for the vortices and turbulent motion, which are expected to be fully three-dimensional. Therefore, as 2D axi-symmetry restricts the motion and changes the character of the turbulence invoked, for the goal of this paper, that is to study the role of turbulent heating, we lift this restriction and employ 3D simulations.

The 3D numerical setting is described in section 2. In sections 3 we present the flow structure, and in section 4 we study the heating of the ICM. Our short summary is in section 5.

2. NUMERICAL SETUP

We use the PLUTO code (Mignone et al. 2007) for the hydrodynamic simulations, in a three-dimensional Cartesian grid with adaptive mesh refinement (AMR). The computational grid is in the octant where the three coordinates x , y and z are positive. At the $x = 0$, $y = 0$ and $z = 0$ planes we apply reflective boundary conditions. The z coordinate is chosen along the initial axis of the jets. In reality two opposite jets are launched simultaneously, such that the flow here is assumed to be symmetric with respect to the $z = 0$ plane, amounting to reflective boundary conditions at $z = 0$. The base computational grid (lowest AMR level) spans the cube $0 \leq x, y, z \leq 50$ kpc, with 16 divisions in each direction. Up to 5 AMR levels are employed with a refinement ratio of 2. Thus, the highest resolution is ≈ 0.1 kpc. The refinement criterion is the default AMR criterion in PLUTO v. 4.1, based on the second derivative error norm (Lohner 1987) of the total energy density.

Heat conduction and viscosity are not included in the simulations. However, local heat conduction is expected to be efficient on scales of $\lesssim 0.1$ kpc (Soker 2010), and therefore is effectively incorporated via the resolution of the simulations and does not need to be included. The conclusions are found not to be sensitive to the resolution. Magnetic fields, also not included in the current numerical study, would in reality prevent global heat conduction, but not local heat conduction. The vortices would entangle field lines, leading to local magnetic field line reconnection and hence allowing local heat conduction.

In this study we examine the increase in the kinetic energy of the ICM. The kinetic energy results from turbulence, sound waves, and gas motion induced by cavity motion, i.e., cavity heating (Nulsen et al. 2007). The dissipation of turbulence (e.g., Zhuravleva et al. 2014) and sound waves (e.g., Shabala & Alexander

2007) heats the gas. We do not include dissipation, but we calculate the increase in the kinetic energy of the ICM and term it in short turbulence. However, it should be kept in mind that it actually includes the energy of sound waves and uplifted gas, hence we do account for sound wave heating and cavity heating. If the dissipation is not 100% efficient in transferring kinetic to thermal energy, then we are overestimating this turbulent energy source for heating. The heating by shock waves is examined directly, as shock dissipation is treated by the numerical code. Heating by cosmic rays, e.g., Guo & Oh (2008), are not included in our simulations at all.

On the outer boundaries we use an outflow boundary condition. At the boundary $z = 0$ we inject into the grid a jet with a half-opening angle of $\theta_j = 70^\circ$ (Sternberg et al. 2007). The jet material is inserted through a circle $x^2 + y^2 \leq r_j^2$ on the $z = 0$ plane with a radius of $r_j = 3$ kpc. The initial jet velocity in the nominal case is $v_j = 8200 \text{ km s}^{-1}$, a Mach number of about 10. The direction of the velocity at each injection point $(x, y, 0)$ in the circle is $\hat{v} = (x, y, h_j) / \sqrt{x^2 + y^2 + h_j^2}$, where $h_j = r_j / \tan \theta_j$. The jet is injected during each active episode, and when the jet is turned off reflective boundary conditions apply in the whole $z = 0$ plane. In the nominal run, the jet is periodically turned on for 10 Myr and off for 10 Myr. The power of the two jets together is

$$\dot{E}_{2j} = 2 \times 10^{45} \text{ erg s}^{-1}, \quad (1)$$

half of it in each direction. The mass deposition rate is thus

$$\dot{M}_{2j} = \frac{2\dot{E}_{2j}}{v_j^2} = 94 M_\odot \text{ yr}^{-1}. \quad (2)$$

In two additional simulations we vary two parameters. In one simulation, termed Run B below, we reduce the jet activity and quiescence time intervals by a factor of 5. In a different simulation, Run C, we increase the velocity by a factor of $\sqrt{10}$ and lower the mass deposition rate, keeping the jet power unchanged.

As we do not include magnetic fields, hence their influence on instabilities, the roles of magnetic fields in the mixing process and in small scale motions are not explored here. Although in two dimensions magnetic fields act to stabilize some instabilities (e.g., Robinson et al. 2004), in three dimensions the magnetic fields cannot suppress instabilities with wave-vector components perpendicular to the field lines. Hence, we do not expect magnetic fields to suppress mixing, but only to influence the details of the mixing. Another effect is that the violent vorticity we find can amplify magnetic fields to the point that they start to reconnect and heat the gas. This overall process channels kinetic energy to magnetic energy and then to thermal energy, hence increasing the heating efficiency of the mixing process. Overall we do not expect magnetic fields to influence the main conclusions of this study.

The simulation begins with an isothermal box of gas at an initial temperature of $T_{\text{ICM}}(0) = 3 \times 10^7 \text{ K}$ with a density profile of (e.g., Vernaleo & Reynolds 2006)

$$\rho_{\text{ICM}}(r) = \frac{\rho_0}{\left[1 + (r/a)^2\right]^{3/4}}, \quad (3)$$

with $a = 100 \text{ kpc}$ and $\rho_0 = 10^{-25} \text{ g cm}^{-3}$. A gravity field is added to maintain an initial hydrostatic equilibrium, and is kept constant in time. We include radiative cooling in the simulations, where the tabulated cooling function is taken from the solar-metalicity values of Table 6 in Sutherland & Dopita (1993).

We run simulations with either 4 or 5 levels of AMR, to check for numerical convergence. We found no noticeable differences in the results. We also run simulations with a twice as large grid and no reflecting

boundary conditions on the plane $x = 0$. Namely, the x -coordinate covers the range $-50 \text{ kpc} \leq x \leq 50 \text{ kpc}$. We found no significant changes in the results, hence conclude that the reflecting boundary conditions do not affect our results, both qualitatively and quantitatively.

3. FLOW STRUCTURE

We begin by presenting in Fig. 1 the flow structure at different times. This high-resolution simulation was run for 50 Myr. To follow the evolution of the same setting for 240 Myr we used a lower resolution grid. In the common time the results of the two runs are similar.

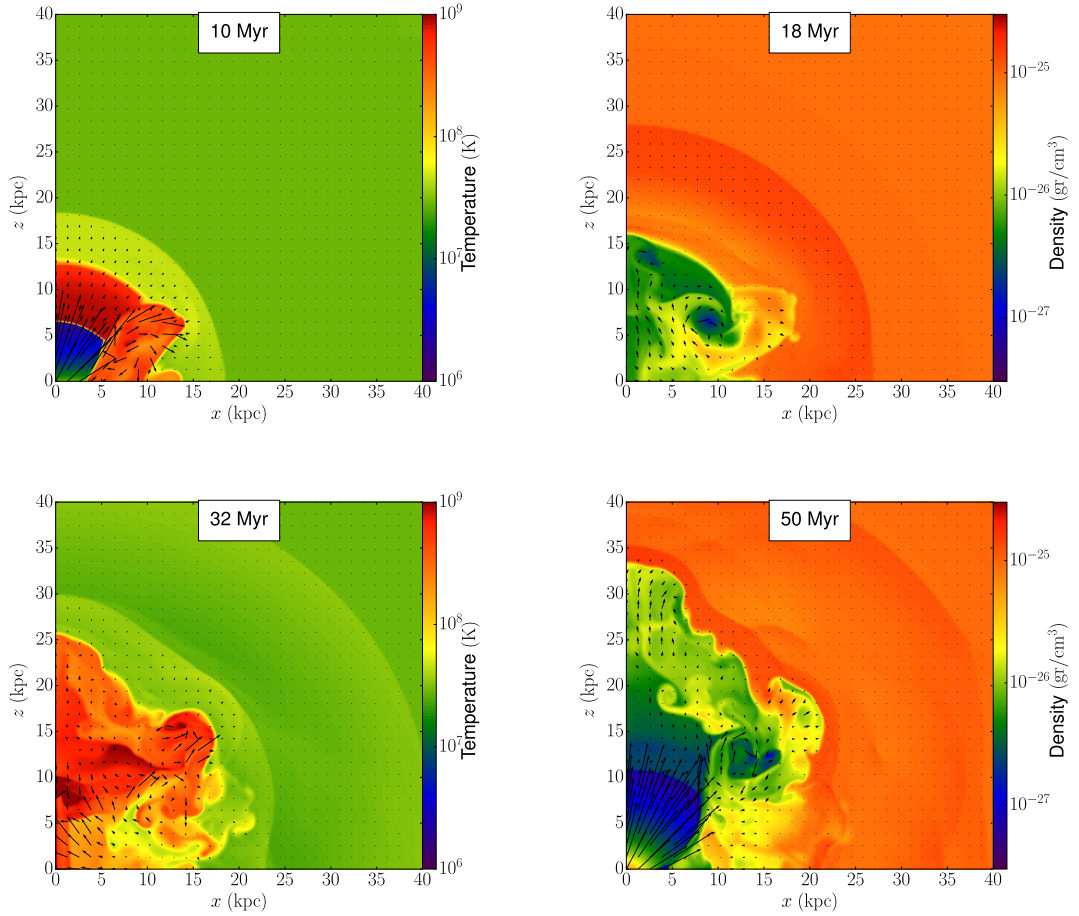


Fig. 1.— Evolution of the flow for the nominal case parameters given in section 2, presented in the meridional plane $y = 0$ at four times. The jet is injected through a circle of radius $r_j = 3 \text{ kpc}$ on the $z = 0$ plane. The half-opening angle is $\theta_j = 70^\circ$, i.e., the jet velocity on the boundary of the circle has an angle of 70° with respect to the z -axis. The left panels present temperature maps and the right panels mass density maps. The color coding of temperature and density is in logarithmic scale. Arrows show the velocity, with length proportional to the velocity magnitude. A length of 1 kpc on the map corresponds to 1700 km s^{-1} . When the jet is active, the length of arrows close to the origin corresponds to 8200 km s^{-1} .

As evident from Fig. 1, e.g., at $t = 32$ Myr, we manage to inflate bubbles which match those seen in observations as X-ray deficient cavities (Sternberg et al. 2007; Hillel & Soker 2014; Gilkis & Soker 2012). The inflation of bubbles similar to those observed in a self-consistent manner is crucial to the study of the different heating mechanisms: mixing, shocks, and the excitation of ICM turbulence that can dissipate later on.

In order to compare to observational data, in the left panel of Fig. 2 we present mock X-ray images of the nominal simulation at time $t = 50$ Myr. This image was created by folding the simulated octant twice, such that the four quarters of the plane are identical. Although the initial setup of the simulation is cylindrically symmetric, hydrodynamic instabilities magnified numerically cause departures from that symmetry. In particular, the surface of the low density hot bubble is ripply and uneven, with several relatively dense filaments crossing that volume near the bubble’s surface (later discussed in relation to Fig. 7). These appear as a net of bright filaments covering the dark (low density) bubble on the left panel of Fig. 2. Present X-ray observations are not sharp enough to detect such filaments. In addition, more sophisticated simulations might have erased these filaments by including realistic local heat conduction.

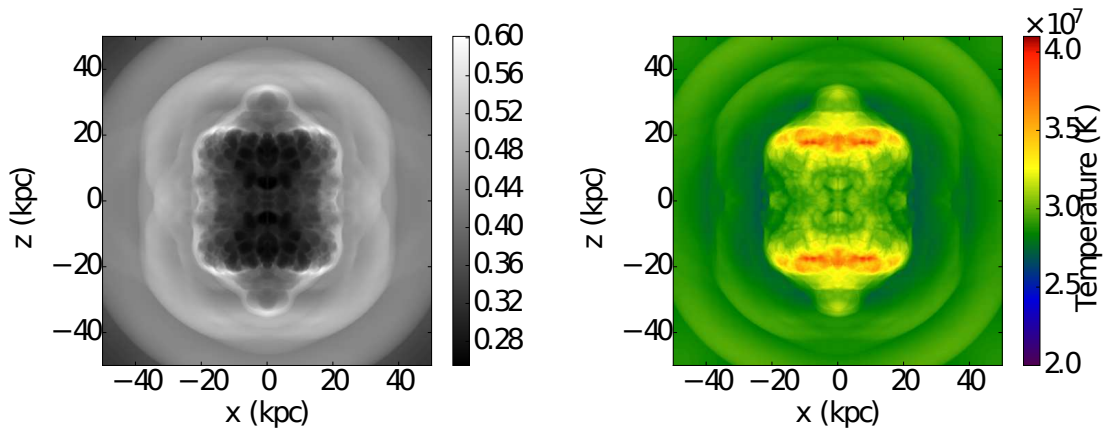


Fig. 2.— Mock X-ray image (left panel) and emission-weighted temperature map (right panel) of the nominal simulation at time $t = 50$ Myr. The simulated octant was folded twice to create these panels. Hence the four quarters about the origin are identical to each other. The X-ray image is created by the integration of the density squared along lines parallel to the y -axis. The units are arbitrary. The emission-weighted temperature map is made by calculating the average, along the line of sight, of the temperature weighted by the emission power, Eq. (4). Note the X-ray deficient bubbles inflated by the jet.

The ‘waist’ between the two bubbles in the plane $z = 0$ obtained here is wider than in typical observed bubbles. Our method of injecting the jet, through a circle on the surface $z = 0$, is one of the causes of the wide waist near $z = 0$. In addition, on the plane $z = 0$ we have reflective boundary conditions which add to the numerical error near the plane. However, overall, we obtain an image which reasonably resembles observations.

The right panel of Fig. 2 is an emission-weight temperature map at the same time, $t = 50$ Myr. The emission-weighted temperature at each point (x, z) in the image is the average of the temperature, along the

line of sight (y -axis here), weighted by the emission power,

$$T_{\text{ew}} = \frac{\int \Lambda(T) n^2 T dy}{\int \Lambda(T) n^2 dy}. \quad (4)$$

For reference we also provide representative shock Mach number values. At the front of the jet, on the z -axis, the first shock wave running through the ICM has a Mach number of $\mathcal{M} = 1.53$ at $z = 20$ kpc and a Mach number of $\mathcal{M} = 1.18$ when it reaches a distance of $z = 40$ kpc. As we show later, such weak shocks are insignificant in heating the ICM.

To better capture some properties of the flow we present artificial flow quantities called ‘tracers’. The tracers are frozen-in to the flow, and hence represent the spreading with time of gas starting in a certain volume. A tracer’s initial value is set to $\xi(0) = 1$ in a certain volume and $\xi(0) = 0$ elsewhere. If the traced gas is mixed with the ICM or the jet’s material, its value drops to $0 < \xi(t) < 1$.

In Fig. 3 we present maps of a tracer that follows the ejected jet material. In the simulation the jet is injected via the boundary condition at $z = 0$ (see section 2), and the injected material is marked with a tracer that follows its evolution throughout the simulation. We plot the tracer distribution in the $y = 0$ meridional plane at two times as indicated in the different panels. Each point in space in which the tracer value is $\xi > 0$ indicates that material from the jet has reached it. We find again that a prominent phenomenon in such simulations of self-consistent bubble inflation is the appearance of vortices and mixing (Gilkis & Soker 2012; Hillel & Soker 2014). The inflation of the bubble by the jet induces a complicated flow structure with multiple vortices, some induced by vortex shedding (Refaelovich & Soker 2012; Walg et al. 2013).

In the upper-left panel of Fig. 3 we present the entire range of $0 \leq \xi \leq 1$, while in the upper-right panel we zoom on a specific region and emphasize the range $0 < \xi < 0.1$. The arrows represent the direction and magnitude of velocity. Too long arrows are truncated with a length corresponding to a maximum velocity v_m as explained in the caption. Vigorous mixing caused by vortices can be seen in these two panels, i.e., the vortex at $(x, z) = (5, 18)$ kpc. In the upper-right panel we can notice jet’s material that reaches the point $(x, z) = (23, 3.5)$ kpc. This clearly shows that the mixing of hot shocked jet’s gas can heat the ICM to large distances in directions perpendicular to the initial jet direction. Considering that in a more realistic scenario the jets precess and eject material in other directions, the mixing is more efficient even than what is found here.

The two lower panels of Fig. 3 present a later evolution time. The curved arrows in the lower-left panel represent stream lines, and the arrows in the lower-right panel represent mass flux $\phi = v\rho$. Both the stream lines and the arrows show a shock expanding outward at $r \approx 35$ kpc. We can see again jet’s material that reaches regions away from the jets’ axis, here at $(x, z) = (28, 20)$ kpc.

In Figs. 4 and 5 we show the evolution of tracers that are frozen-in to the ICM. In both cases the tracer follows the gas that started in a torus around the z axis, and the radius of the cross section of the torus is 2.5 kpc. In Figs. 4 we follow the tracers whose torus cross section is centered at $(x, z) = (10, 5)$ kpc, and in Fig. 5 whose torus cross section is centered at $(x, z) = (20, 15)$ kpc. The bottom right panel of Fig. 5 shows the tracer of the jet rather than the tracer of the ICM. Both figures clearly show the efficient mixing of the ICM with the hot bubble gas.

The tracer in Fig. 4 is initially pushed outward by the outgoing shock waves and the growing bubble of hot gas that induces sound waves. However, at $t \approx 40$ Myr it begins to be mixed with hot jet gas, as the large vortex induced by bubble inflation tears it apart. At $t \approx 100 - 150$ Myr it becomes almost completely mixed with its surroundings as well as with the jet gas.

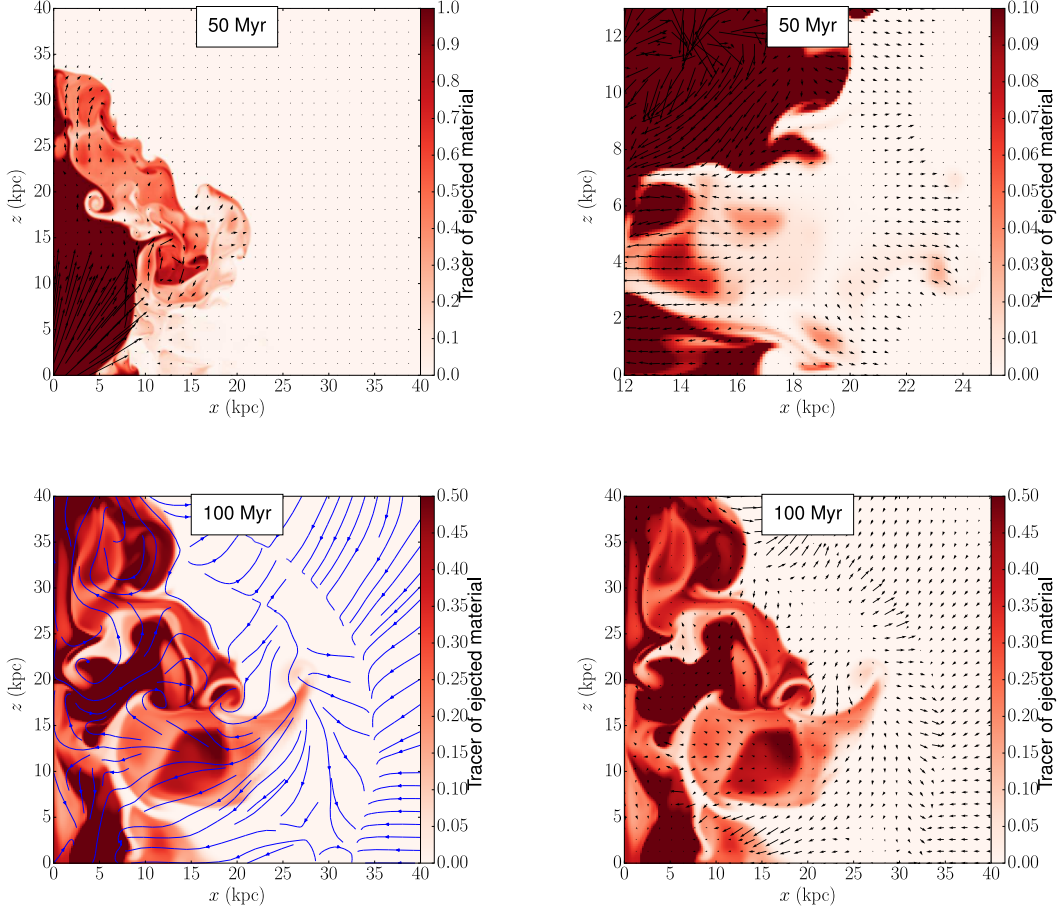


Fig. 3.— A $y = 0$ slice of the tracer that is frozen-in to the jet material, at times $t = 50$ and 100 Myr in a simulation with the same parameters as in Fig. 1. The value of the tracer is color-coded according to the scale shown on the right of each panel. In two panels the length of the arrow is linear with velocity up to an upper limit v_m . In the upper-left panel the largest velocity arrow corresponds to $v_m = 8200 \text{ km s}^{-1}$, the initial jet velocity. Faster regions are presented with an arrow length corresponding to $v_m = 8200 \text{ km s}^{-1}$. The upper-right panel zooms on a region away from the center to emphasize mixing of jet’s material away from the center and near the equatorial plane. The largest velocity arrow corresponds to $v_m = 3000 \text{ km s}^{-1}$. In the lower-left panel we show stream lines of the flow at $t = 100$ Myr, and in the lower-right panel we show mass flux arrows, i.e., $\phi = v\rho$. A length of 1 kpc on the map corresponds to $\phi = 2.3 \times 10^{-23} \text{ km s}^{-1} \text{ g cm}^{-3}$.

The tracer of the gas starting further out and presented in Fig. 5 follows a similar pattern, but begins to be mixed with the hot bubble gas at much later times. Even that it is pushed out to $\approx 30 \text{ kpc}$, it eventually flows inward and mixes with the hot bubble gas and heats up, as we show in section 4. In the lower-right panel of Fig. 5 we show the tracer of the jet. The two lower panels that are given at the same time clearly present the efficient mixing of the ICM and the hot bubble gas. For example, a clear vortex mixing the two media is seen circulating around $(x, z) = (17, 5) \text{ kpc}$.

An inflow of gas near the equatorial plane is seen at the latest time in Fig. 5. This carries ICM gas

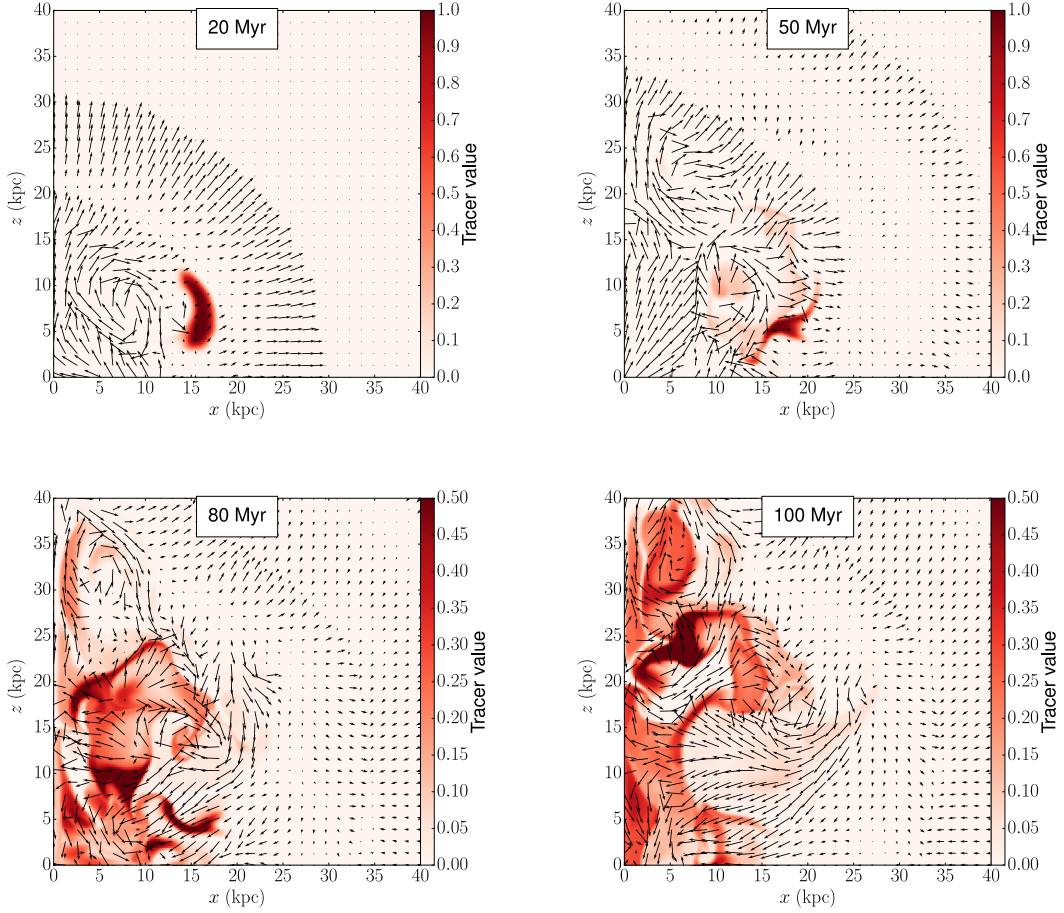


Fig. 4.— Evolution with time of the gas that at $t = 0$ was contained in a torus whose axis is the z -axis and whose cross section is a circle centered at $(x, z) = (10, 5)$ kpc with a radius of $r = 2.5$ kpc. Shown is the concentration of this gas, as followed by its tracer, in the meridional plane $y = 0$ at four times. Flow parameters are as in previous figures. The largest velocity vector corresponds to $v_m = 400 \text{ km s}^{-1} \simeq 0.5 \mathcal{M}_{\text{ICM}}$, where \mathcal{M}_{ICM} is the Mach number in the ICM. Higher velocities are marked with arrows with the same length as that of v_m .

toward the jets, followed by mixing and heating. This demonstrates again that the jets can heat material even in regions further out and near the equatorial plane. If the jets continue to be active for a very long time along the same axis, a massive meridional flow will develop in the ICM (Soker et al. 2015). This flow carries cooler ICM gas towards the center and mixes it with the hot bubble gas. This is an indirect mechanism by which a jet may heat up gas in regions further away from its axis.

4. HEATING THE ICM

We turn to present the energy history of the ICM. In order to follow specific regions we mark them with ‘tracers’ as explained in section 3. The total mass of a traced gas is given by the sum $M_{\text{tr}} = \sum \xi_i M_i$

over all grid cells. As the tracers are advected with their associated mass, the total traced mass is constant with time, as long as traced gas does not leave the grid. Since there are outflow boundary conditions on the grid faces $x = 50$ kpc, $y = 50$ kpc and $z = 50$ kpc, and traced gas is dragged by the jets after some time, traced gas does eventually leave the grid. When that happens we stop following the thermal evolution of that traced gas.

We use the tracers to define the total energy E_{tr} of a traced region as

$$E_{\text{tr}} \equiv \sum_i \xi_i E_i, \quad (5)$$

where i runs over all grid cells. In this work, E_{tr} stands for the traced gas’s total kinetic energy, internal energy, or gravitational energy, and E_i stands for the corresponding energy in cell i . In Fig. 6 we present the energy histories of different traced regions in the simulations. The internal energy and the gravitational energy are drawn with respect to their initial value which is different than zero. The initial kinetic energy is zero. The initial thermal energy of each traced region is given in the caption.

In addition to the nominal jet parameters specified in sections 2 and 3, we conducted two simulations with varying parameters, in order to check the robustness of our conclusions. The nominal simulation is represented in the three panels in the left-hand column of Fig. 6. Two additional simulations, Run B and Run C, are represented in the middle and right-hand columns respectively. We shall elaborate on them below.

Consider first the results of the nominal simulation, i.e., the left-hand column. In the panels in the top row of Fig. 6 we present the energy evolution of mass located at $t = 0$ inside a sphere of radius $r = 15$ kpc centered at the origin. Because of the structure of our grid, only an eighth of the sphere is traced. The initial internal energy of this traced gas in the simulated eighth is $E_{\text{in}}(0) = 3.1 \times 10^{58}$ erg, such that the maximum value of the extra thermal energy in the plot is $\Delta = [E_{\text{in}}(\text{max}) - E_{\text{in}}(0)]/E_{\text{in}}(0) = 390\%$ (in the nominal case) above the initial internal energy. The calculation is stopped when traced gas starts leaving the computational grid.

The panels in the middle row present the energy history of the traced gas whose spreading history is displayed in Fig. 4. In this case $E_{\text{in}}(0) = 5.5 \times 10^{57}$ erg, and $\Delta = [E_{\text{in}}(\text{max}) - E_{\text{in}}(0)]/E_{\text{in}}(0) = 550\%$ (in the nominal case). The calculation is stopped when traced gas starts leaving the computational grid. The panels in the bottom row present the energy history of the traced mass whose spreading history is shown in Fig. 5. In this case $E_{\text{in}}(0) = 1.1 \times 10^{58}$ erg, and $\Delta = [E_{\text{in}}(\text{max}) - E_{\text{in}}(0)]/E_{\text{in}}(0) = 50\%$ (in the nominal case).

A general characteristic behavior emerges from the energy evolution of the traced masses presented here, as well as of other traced regions we have studied but left out of this text. The variation on a time scale of 20 Myr corresponds to the time period of the jet activity. Each active phase lasts for 10 Myr, followed by a quiescence phase of 10 Myr. The periodic jet activity induces gas motion in the ICM such that the kinetic energy of the ICM at each point varies with time. This variation is more or less in a periodic manner, with only a moderate increase in the kinetic energy over several periods. The gravitational energy changes by a negligible amount compared to both the kinetic and internal energies. The main energy increase over several periods comes from an increase of the internal energy.

Consider the middle panel in the left-hand column of Fig. 6, which shows the energy history of the tracer presented in Fig. 4. There are some variations due to two shock waves that pass through the traced region. The shocks increase the internal energy, but the gas re-expands and the net thermal energy gain is negligible. This traced mass begins to mix with hot bubble gas at $t \approx 40$ Myr. From that time on the

mean internal energy increases significantly. The upper right panel of Fig. 4 shows the traced gas at time $t = 50$ Myr, while both upper panels of Fig. 3 show the presence of the jet material at the same time. It is apparent that the hot shocked jet (bubble) gas is being mixed vigorously with the ICM gas marked by the tracer. The mixing is facilitated by the vortices induced by the jet-inflated bubble.

Similar heating by mixing happens in the tracer presented in Fig. 5, whose energy history is shown in the bottom panel in the left-hand column of Fig. 6. Periodic heating by shocks is clearly seen, although over a long time shocks cannot compete with radiative cooling. Indeed, at early times the internal energy decreases. Here the mixing begins at $t \sim 110$ Myr. In the $t = 100$ Myr panel of Fig. 5 we can see a vortex that is just about to touch the traced region and mix it with hot bubble gas that can be seen in the $t = 100$ Myr panel of Fig. 3.

The heating is mainly due to mixing of the ICM gas with shocked jet material, i.e., the hot bubble gas. Both the mixing that leads to an increase in internal energy and the turbulent energy are driven by vortices. It is hard to estimate directly the amount of turbulent kinetic energy of the ICM from the simulations, because the grid resolution is not high enough to capture all relevant scales. However, we give rough arguments that the kinetic energy we calculate is not much smaller than the corresponding ‘true’ turbulent energy. Firstly, the kinetic energy is calculated with respect to the center of mass of the whole system, and not with respect to a local mean flow of the gas. Thus, it overestimates the turbulent energy as it is usually defined. Secondly, our calculated kinetic energy does not properly include the kinetic energy in smaller scales than the grid resolution, and thus it underestimates the turbulent kinetic energy. However, the kinetic energy is mainly due to vortices which are significantly larger than the grid resolution. Therefore, we do not expect that the underestimation of the turbulent kinetic energy in small unresolved scales is significant. Thirdly, some of the kinetic energy we count is due to sound waves that propagate out and do not heat the inner region. Finally, motion in smaller scales is less energetic, and it also tends to dissipate to internal energy.

We now turn to the additional two simulations presented in Fig. 6. In one simulation, Run B, shown in the panels in the middle column of Fig. 6, the jet is periodically turned on for 2 Myr and off for 2 Myr, instead of 10 Myr/10 Myr in the nominal run. Density, temperature, and velocity maps in the $y = 0$ plane at time $t = 50$ Myr of Run B are shown in the middle column of Fig. 7. In Run C, shown in the panels in the right-hand column of Fig. 6, the jet periodicity is unchanged, but the mass deposition rate is decreased by a factor of 10 and the jet velocity is increased by a factor of $\sqrt{10}$ with respect to the nominal simulation. The rest of the parameters are as in the nominal simulation. The flow maps for Run C in the $y = 0$ plane at $t = 50$ Myr are shown in the right-hand side column of Fig. 7. In all simulations the mean jet power is the same, Eq. (1).

The detailed flow and vortex structure in the three simulations is dependent upon the parameters in a complicated way. However, we can draw conclusions which do not depend on the exact value of the parameters. In Run B (middle column of Fig. 6), the time period of jet episode activity is 5 times shorter. The immediate effect seen is the smaller and more frequent ‘bumps’ as a result of the shock waves. In addition, the shape of the hot bubble is elongated in the direction of the axis of the jet, while maintaining a similar volume which depends only on the jet energy output. Run C, with the higher jet velocity and lower mass deposition rate, has a similar general structure to the nominal run, but the details are different. In Run C there is less momentum per unit mass and per unit energy, compared with the nominal run. The bubble front along the z -axis after 50 Myr extends only to 27 kpc, compared with 32 kpc in the nominal run. The vortex on the right side of the bubble in Fig. 7 is larger in Run C than in the nominal run. The waist in Run C is wider than in the nominal run. The nominal run better matches the morphology of observed bubbles.

This is one of the reasons we use slow jets (Sternberg et al. 2007). Another reason is recent observations of such outflows from AGN (e.g., Chamberlain et al. 2015).

The energy histories of the traced regions in these simulations, Fig. 6, is similar to the nominal run with the following exceptions. In Run B (middle column of Fig. 6), in the tracer shown in the bottom panel, the traced gas gets close to the hot bubble at $t = 100 - 150$ Myr but does not mix with the hot gas. The more frequent episodes create less vortices and in fact push out the traced gas almost continuously. In contrast, in the nominal run, where the jet is periodically turned on and off for 10 Myr, the longer quiescence time allows for the cooled ICM gas to be pulled in to the center and thus to heat up by mixing with the hot bubble gas. In Run B this happens to a lesser extent. Thus, the traced ICM gas remains in the dense shell surrounding the hot bubble, which in turn radiates its energy more efficiently. This radiative cooling is the cause of the decline of internal energy starting at time $t \approx 180$ Myr. As seen in this example, more shock waves (keeping the jet power fixed) may, in some cases, actually heat some of the ICM gas less efficiently, because it pushes the gas out more continuously, which inhibits mixing.

Similar cooling of the same traced region happens in Run C, as seen in the bottom-right panel of Fig. 6. Here, the gas begins to mix at time $t \approx 110$ Myr, as in the nominal simulation. However, the slightly different vortex structure does not pull in the entirety of the traced gas and most of it remains out of the hot bubble, in the surrounding dense shell. Thus, as in Run B, it loses internal energy quickly by radiative cooling. This may be a mechanism for feeding the AGN by cold gas. ICM gas gets pulled in to the center during quiescence periods because of the lower pressure in the hot bubble, cools radiatively when its density increases, and is then pulled in further. At this stage it either heats up or cools further and falls in to feed the AGN.

The main results from the comparison of the different cases is as follows. Because of the different flow structure in simulations with varying parameters, some of the gas heats up more and some less, depending on the location of the gas, but mixing is the main heating process among those probed in the simulations.

We thus conclude by arguing that mixing, due to vortices, is more important as a heating process of the ICM gas by jets than turbulent heating and shock heating. Shock waves induce an expansion and contraction and increase kinetic energy by creating motion, but their contribution to the heating is largely temporary and almost periodic in our setting. Turbulent motion is also not the main heating mechanism, although it might carry up to ≈ 0.2 of the energy transferred from the jets to the ICM.

5. SUMMARY

Motivated by the recent claim of Zhuravleva et al. (2014) that turbulent-heating can counter radiative cooling in the cooling flow clusters Virgo and Perseus, we compare the energy channeled from jets to ICM turbulence with the direct thermal heating by mixing hot bubble gas with the ICM. We have done so by conducting 3D hydrodynamical simulations of wide jets that inflate bubbles. We used the PLUTO (Mignone et al. 2007) hydrodynamical code in Cartesian coordinates.

The inflation of bubbles leads to the development of vortices in the entire volume around the expanding jets and bubbles, as can be seen in Figs. 1-5 and 7. These vortices excite turbulence in the ICM. These vortices also efficiently mix ICM gas with the hot bubble gas. This mixing can best be seen in Fig. 4 where the tracer (colored red) of ICM gas located initially within a torus is seen to be mixed with the bubble gas.

We use slow massive wide (SMW) outflows. Such flows are supported by observational findings (e.g.,

Chamberlain et al. 2015 and references therein). In many cases outflows from AGN include relativistic components. By comparing the results of Run C with the nominal run, e.g., in Fig. 7, we note that when the velocity is three times as high, the bubble stays wide and a large vortex exists on its side. Higher velocities do not change the mixing part by much when wide (fat) bubbles are inflated. Therefore, we do not expect that relativist outflow will change our present conclusions, as long as wide bubbles are inflated. For that, either the jets are wide, or there is a relative transverse velocity between the jets and the ICM, e.g., motion of the AGN relative to the ICM and/or jets’ precession (Sternberg & Soker 2008a). Well-collimated relativistic jets without transverse velocity relative to the ICM will not heat the ICM efficiently away from their propagation cone. They will penetrate to large distances. They can form radio lobes at large distances, but will not heat the ICM close to the center.

We then compared the increase in thermal energy of the ICM medium we trace, with the increase of its kinetic energy. We found that the energy channeled to directly heating the gas is more than 3 times larger than that channeled to kinetic energy of the ICM, and typically larger than 4 times the kinetic energy. This is our main result and it is presented in Fig. 6. As only part of the kinetic energy will turn to turbulence (some is just large-scale motion), we conclude that turbulent-heating is $\lesssim 30\%$ as efficient as mixing-heating. Heating by shocks is very small, as was shown in 2D simulations (Gilkis & Soker 2012; Hillel & Soker 2014), and was reinforced here in 3D simulations. The significance of the new 3D simulations is that the vortices and turbulent motion is not artificially confined to be cylindrically symmetric. Although the setup is cylindrically symmetric, small perturbations and numerical errors are magnified by hydrodynamic instabilities, and the flow is fully three-dimensional. This is the main difference observed in the 2D and 3D simulations. The conclusions regarding the heating mechanisms, nonetheless, are similar.

It is important to note that since by our finding turbulence carries $\lesssim 25\%$ of the energy deposited by the jets in the inner region, turbulence may still be non-negligible in the ICM, as was found recently by Zhuravleva et al. (2014), Zhuravleva et al. (2015), Arévalo et al. (2015), and marginally by Anderson & Sunyaev (2015). However, since only a portion of the kinetic energy develops to turbulence, and since the total injected jet energy can be channeled into other forms of energy, in some cases turbulence might be insignificant.

Zhuravleva et al. (2014) find observationally that turbulence is present and significant in the ICM, and that the rate of turbulent heating matches the rate of radiative cooling. In contrast, in our simulations we have found that heating by mixing is more significant. Our results further show that a non-negligible amount of energy ends up as kinetic energy of the ICM. However, substantial heating occurs only when mixing takes place. In addition, we find large density fluctuations induced in the ICM by the mixing process and bubble motion; this is best seen in the upper panels of Fig. 7. It seems that a large fraction of the kinetic energy is not turbulent motion that dissipates. The kinetic energy and density fluctuations are associated also with the bubble activity and global gas motion; only part of the kinetic energy belongs to the universal turbulent cascade that Zhuravleva et al. (2014) refer to. Zhuravleva et al. (2014) write: “It is difficult to prove unambiguously that we are dealing with a universal turbulent cascade, as other structures (e.g., edges of the bubbles, entrainment of hot bubble matter, sound waves, mergers and gas sloshing) might also contribute to the observed density-fluctuation spectra.” We suggest that the discrepancy between the claim of Zhuravleva et al. (2014) for efficient turbulent heating and our finding results from a large fraction of the density perturbations and turbulent energy that is indeed in the other structures listed by them. This definitely deserves further investigation.

We thank an anonymous referee for very valuable suggestions and comments.

REFERENCES

- Anderson, M., E., & Sunyaev, R. 2015, arXiv:1506.01703
- Arav, N., Borguet, B., Chamberlain, C., Edmonds, D., & Danforth, C. 2013, MNRAS, 436, 3286
- Arévalo, P., Churazov, E., Zhuravleva, I., Forman, W. R., & Jones, C. 2015, arXiv:1508.00013
- Banerjee, N. & Sharma, P. 2014, arXiv:1403.3395
- Blanton, E. L., Randall, S. W., Clarke, T. E., Sarazin, C. L., McNamara, B. R., Douglass, E. M., McDonald, M. 2011, ApJ, 737, 99
- Brüggen, M., Heinz, S., Roediger, E., Ruszkowski, M., & Simionescu, A. 2007, MNRAS, 380, L67
- Cavagnolo, K. W., McNamara, B. R., Wise, M. W., Nulsen, P. E. J., Brüggen, M., Gitti, M., & Rafferty, D. A. 2011, ApJ, 732, 71
- Chamberlain, C., Arav, N., & Benn, C. 2015, MNRAS, 450, 1085
- David, L. P., Jones, C., Forman, W., Nulsen, P. E. J., Vrtilek, J., O’Sullivan, E., Giacintucci, S., Raychaudhury, S. 2009, ApJ, 705, 624
- Dong, R., Rasmussen, J., & Mulchaey, J. S. 2010, ApJ, 712, 883
- Dunn, J. P., Bautista, M., Arav, N., et al. 2010, ApJ, 709, 611
- Edge, A. C., et al. 2010, A&A, 518, L47
- Fabian, A. C. 2012, ARAA, (arXiv:1204.4114)
- Falceta-Goncalves, D., Caproni, A., Abraham, Z., Teixeira, D. M., & de Gouveia Dal Pino, E. M. 2010, ApJ, 713, L74
- Farage, C. L., McGregor, P. J., & Dopita, M. A. 2012, ApJ, 747, 28
- Fogarty, K., Postman, M., Connor, T., Donahue, M., & Moustakas, J. 2015, arXiv:1509.00487
- Gaspari, M., Brighenti, F., & Temi, P. 2012a, MNRAS, 424, 190
- Gaspari, M., Ruszkowski, M., & Sharma, P. 2012b, ApJ, 746, 94
- Gilkis, A., & Soker, N. 2012, MNRAS, 427, 1482
- Gitti, M., O’Sullivan, E., Giacintucci, S., David, L. P.; Vrtilek, J., Raychaudhury, S., Nulsen, P. E. J. 2010, ApJ, 714, 758
- Guo, F., & Oh, S. P. 2008, MNRAS, 384, 251
- Heinz, S., & Churazov, E. 2005, ApJ, 634, L141
- Hillel, S., & Soker, N. 2014, MNRAS, 445, 4161
- Li, Y., Bryan, G. L., Ruszkowski, M., Voit, G. M., O’Shea, B. W., & Donahue, M. 2015, arXiv:1503.02660
- Lohner, R. 1987, Computer Methods in Applied Mechanics and Engineering, 61, 323

- McCourt, M., Sharma, P., Quataert, E., & Parrish, I. J. 2012, MNRAS, 419, 3319
- McNamara, B. R., & Nulsen, P. E. J. 2007, ARA&A, 45, 117
- McNamara, B. R., & Nulsen, P. E. J. 2012, New Journal of Physics, 14, 055023
- McNamara, B. R., Russell, H. R., Nulsen, P. E. J., et al. 2014, ApJ, 785, 44
- Mendygral, P., Jones, T., & Dolag, K. 2012, ApJ, 750, 166
- Mignone, A., Bodo, G., Massaglia, S., et al. 2007, ApJS, 170, 228
- Moe, M., Arav, N., Bautista, M. A., & Korista, K. T. 2009, ApJ, 706, 525
- Morsony, B. J., Heinz, S., Brüggen, M., & Ruszkowski, M. 2010, MNRAS, 407, 1277
- Nesvadba, N. P. H., Boulanger, F., Lehnert, M. D., Guillard, P., & Salome, P. 2011, A&A, 536, L5
- Nulsen, P. E. J., Jones, C., Forman, W. R., et al. 2007, Heating versus Cooling in Galaxies and Clusters of Galaxies, 210
- Omma, H., Binney, J., Bryan, G., & Slyz, A. 2004, MNRAS, 348, 1105
- O’Sullivan, E., Giacintucci, S., David, L. P., Gitti, M., Vrtilek, J. M., Raychaudhury, S., Ponman, T. J. 2011, ApJ, 735, 11
- Pandge, M. B., Vagshette, N. D., David, L. P., & Patil, M. K. 2012, MNRAS, 421, 808
- Pfrommer, C. 2013, ApJ, 779, 10
- Pizzolato, F. & Soker, N. 2005 ApJ, 632, 821
- Pizzolato, F., & Soker, N. 2010, MNRAS, 408, 961
- Pope, E. C. D. 2009, MNRAS, 395, 2317
- Prasad, D., Sharma, P., & Babul A. 2015, arXiv:1504.02215
- Randall, S. W., Nulsen, P. E. J., Jones, C., et al. 2015, arXiv:1503.08205
- Refaelovich, M., & Soker, N. 2012, ApJ, 755, L3
- Revaz, Y., Combes, F., & Salomé, P. 2008, A&A, 477, L33
- Robinson, K., Dursi, L. J., Ricker, P. M., et al. 2004, ApJ, 601, 621
- Roediger, E., Brüggen, M., Rebusco, P., Böhringer, H., & Churazov, E. 2007, MNRAS, 375, 15
- Russell, H. R., Fabian, A. C., McNamara, B. R., & Broderick, A. E. 2015, MNRAS, in press
- Shabala, S., & Alexander, P. 2007, Ap&SS, 311, 311
- Sharma, P., McCourt, M., Quataert, E., & Parrish, I. J. 2012, MNRAS, 420, 3174
- Soker, N. 2009, MNRAS, 398, L41
- Soker, N. 2010, arXiv:1007.2249

- Soker, N., Akashi, M., Gilkis, A., Hillel, S., Papish, O., Refaelovich, M., & Tsebrenko, D. 2013, *Astronomische Nachrichten*, 334, 402
- Soker, N., Hillel, S., & Sternberg, A., in preparation
- Sternberg, A., Pizzolato, F. & Soker N. 2007, *ApJ*, 656, L5
- Sternberg, A., & Soker N. 2008a, *MNRAS*, 384, 1327
- Sternberg, A., & Soker, N. 2008b, *MNRAS*, 389, L13
- Sutherland, R. S., & Dopita, M. A. 1993, *ApJS*, 88, 253
- Tremblay, G. R., O’Dea, C. P., Baum, S. A. et al. 2015, *MNRAS*
- Vernaleo, J. C., & Reynolds, C. S. 2006, *ApJ*, 645, 83
- Voit, G. M., & Donahue, M. 2015, *ApJ*, 799, LL1
- Voit, G. M., Donahue, M., Bryan, G. L., & McDonald, M. 2015, *Nature*, 519, 203
- Wagh, B., Sharma, P., & McCourt, M. 2014, *MNRAS*, 439, 2822
- Walg, S., Achterberg, A., Markoff, S., Keppens, R., & Meliani, Z. 2013, *MNRAS*, 433, 1453
- Wilman, R. J., Edge, A. C., McGregor, P. J., & McNamara, B. R. 2011, *MNRAS*, 416, 2060
- Zhuravleva, I., Churazov, E., Arevalo, P., et al. 2015, *arXiv:1501.07271*
- Zhuravleva, I., Churazov, E., Schekochihin, A. A., et al. 2014, *Nature*, 515, 85

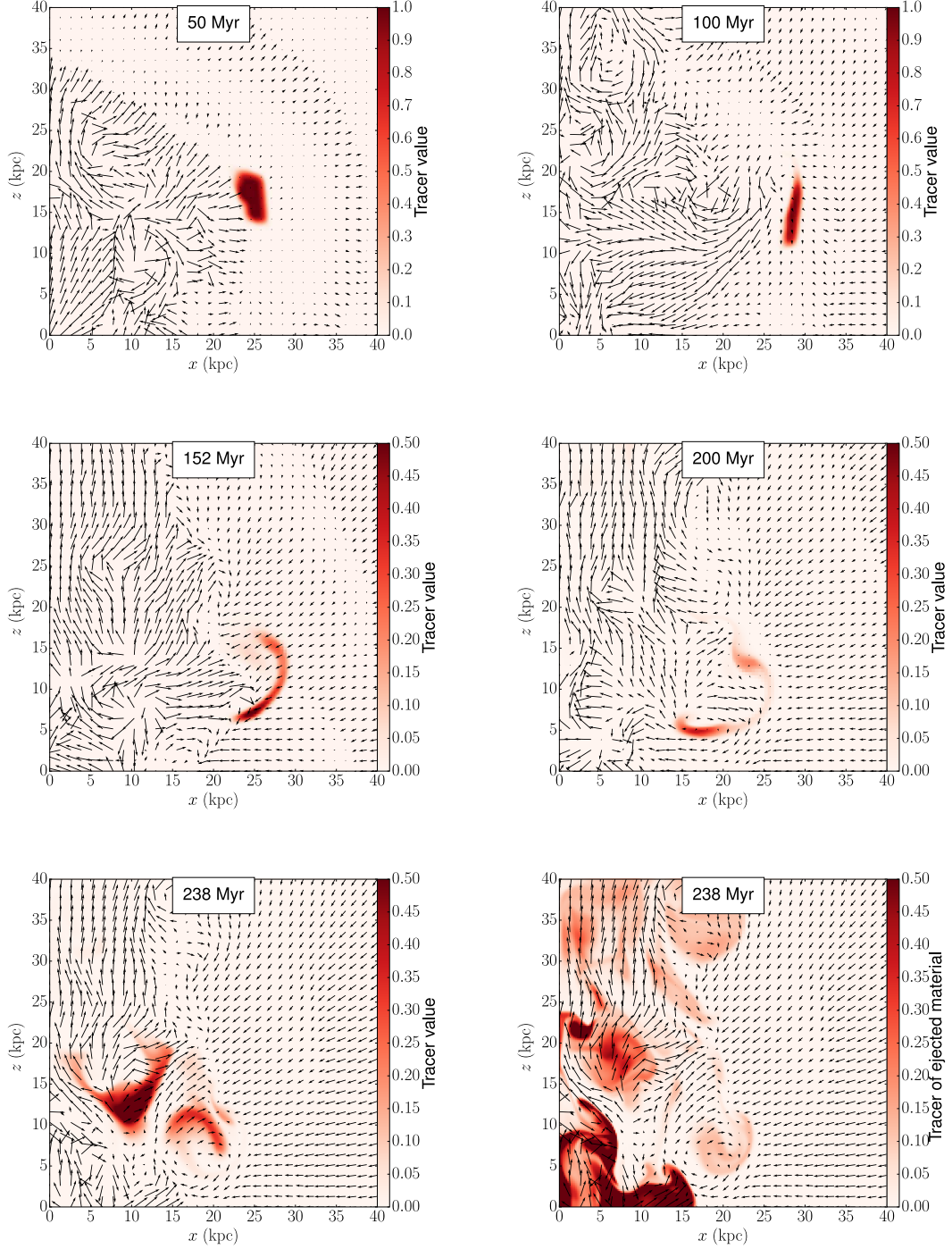


Fig. 5.— Evolution with time of the gas that at $t = 0$ was contained in a torus whose axis is the z -axis and whose cross section is a circle centered at $(x, z) = (20, 15)$ kpc with a radius of $r = 2.5$ kpc. In the first five panels the concentration of this gas, as followed by its tracer, is shown in the meridional plane $y = 0$ at five times. The lower-right panel shows the tracer of the jet. Flow parameters as in previous figures. The largest velocity vector corresponds to $v_m = 400 \text{ km s}^{-1}$, a Mach number of about 0.5. Higher velocities are marked with arrows with the same length as that of v_m .

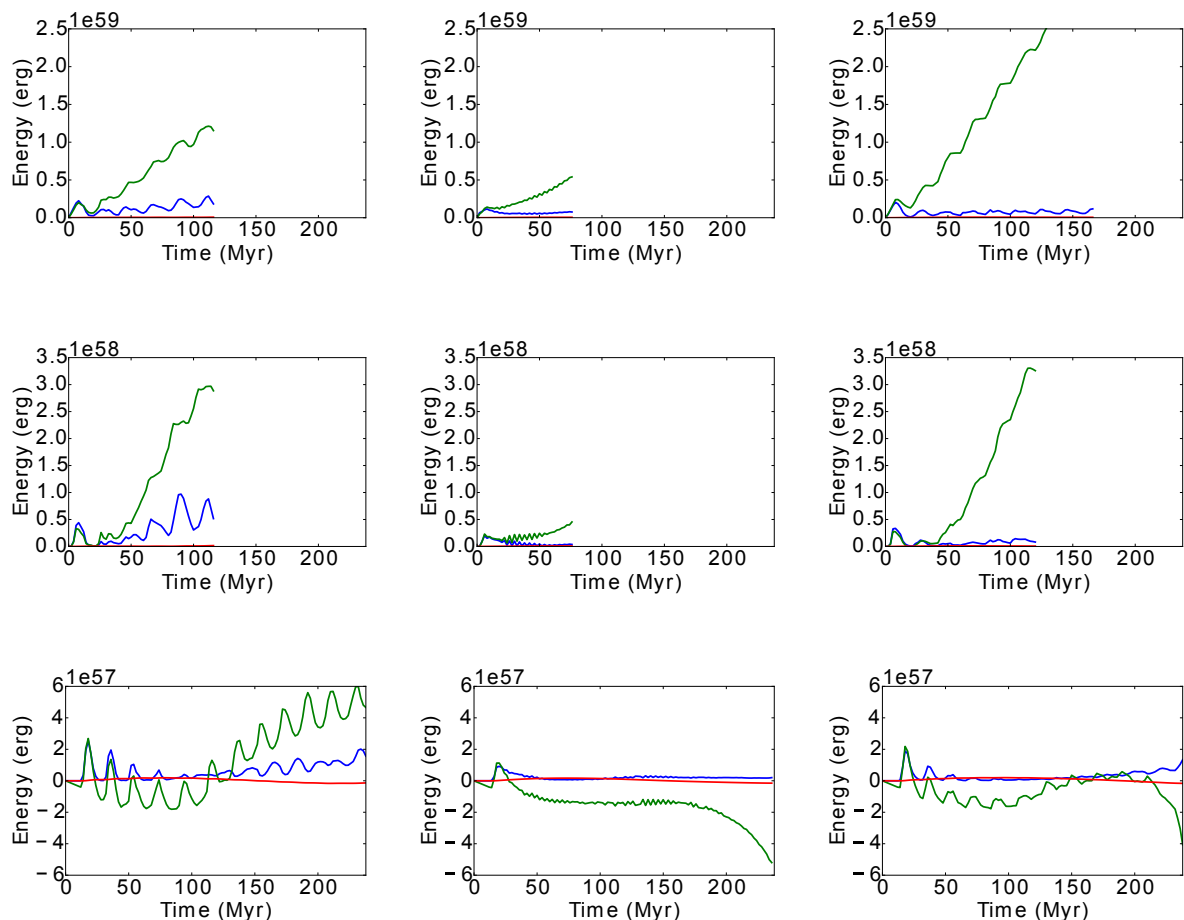


Fig. 6.— The energy history of different traced regions of the nominal simulation studied here as well as in two additional simulations. The three panels in the left-hand column represent the nominal simulation. In the second simulation, Run B, presented in the middle column, the jet is periodically turned on for 2 Myr and off for 2 Myr. The rest of the parameters are as in the nominal simulation used in the rest of this work. In the third simulation, Run C, presented in the right-hand column, the jet mass deposition rate is decreased by a factor of 10 and the jet velocity is increased by a factor of $\sqrt{10}$ with respect to the nominal simulation, such that the jet’s power is unchanged. Otherwise, the setup is the same. In the three panels in the top row we present the evolution with time of three energy components of the ICM gas that starts (before the jets become active) inside an eighth of ball with $r = 15$ kpc centered at the origin. It is an eighth of a ball as we simulate one eighth of the space. The green line in each panel represents the internal energy, the blue line represents the kinetic energy, and the red line represents the gravitational energy of this traced gas. The middle-row panels show the energy histories of the torus shown in Fig. 4, and the panels in the bottom row show the energy histories of the torus shown in Fig. 5. All energies are shown relative to their values at $t = 0$. The initial internal energies $E_{\text{in}}(0)$ of the traced regions, from top to bottom, are 3.1×10^{58} erg, 5.5×10^{57} erg and 1.1×10^{58} erg, respectively. The top- and middle-row panels are cut off at the time when the traced material starts leaving the grid.

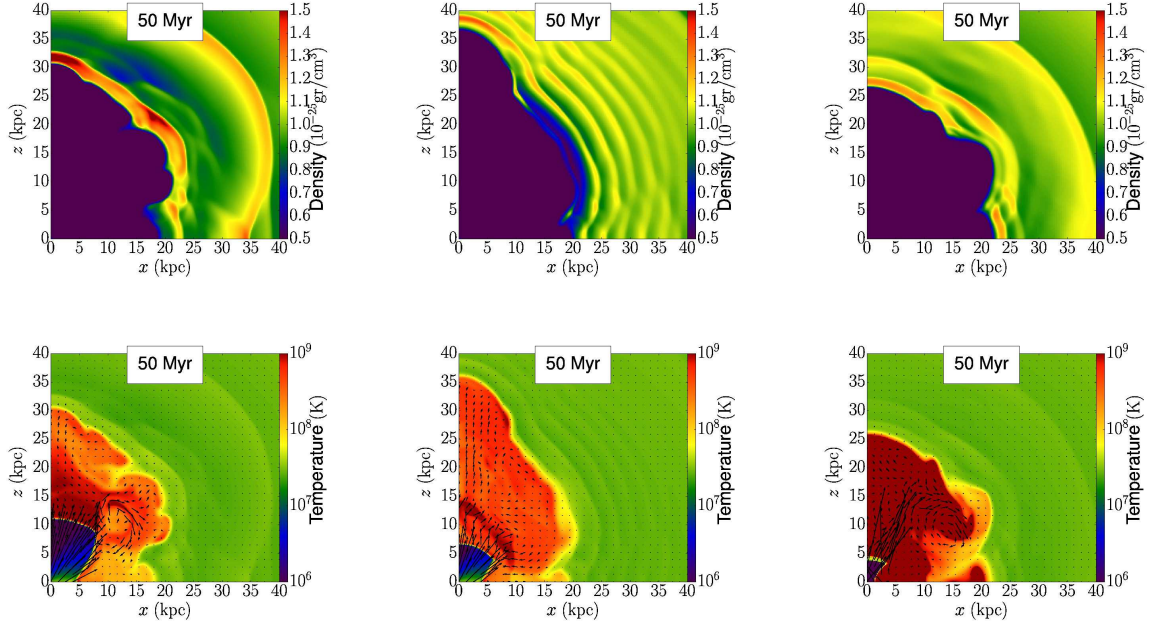


Fig. 7.— Mass density and temperature maps of the nominal run (left column), Run B (middle column) and Run C (right column) whose energy histories are presented in Fig. 6. The $y = 0$ slices of the simulations are presented at time $t = 50$ Myr. The color coding of the density is linear and presented in the range $(0.5, 1.5) \times 10^{-25} \text{ g/cm}^3$, and the temperature coding is in logarithmic scale. Arrows represent the velocity, where a length of 1 kpc on the map corresponds to 1700 km s^{-1} .